

Self-Organization of Plasmonic and Excitonic Nanoparticles into Resonant Chiral Supraparticle Assemblies

Tao Hu,^{†,‡} Benjamin P. Isaacoff,[§] Joong Hwan Bahng,^{†,||} Changlong Hao,[⊥] Yunlong Zhou,^{†,||} Jian Zhu,^{†,||} Xinyu Li,^{†,‡} Zhenlong Wang,[‡] Shaoqin Liu,[‡] Chuanlai Xu,[⊥] Julie S. Biteen,^{*,○} and Nicholas A. Kotov^{*,†,‡,||,#}

[†]Department of Chemical Engineering, [§]Applied Physics Program, ^{||}Biointerfaces Institute, [#]Department of Materials Science and Engineering, and [○]Department of Chemistry, University of Michigan, Ann Arbor, Michigan 48109, United States

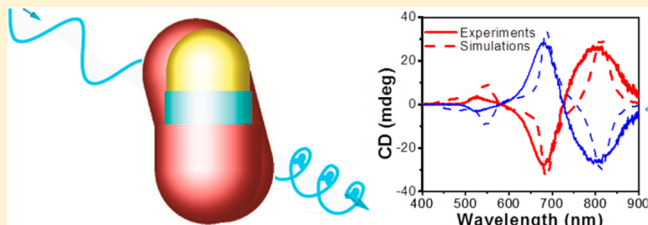
[‡]Key Laboratory of Microsystems, Micronanostructures Manufacturing, Ministry of Education, Harbin Institute of Technology, Harbin 150080, P. R. China

[⊥]State Key Lab of Food Safety and Technology, School of Science and Technology, Jiangnan University, Wuxi, JiangSu, 214122, P. R. China

S Supporting Information

ABSTRACT: Chiral nanostructures exhibit strong coupling to the spin angular momentum of incident photons. The integration of metal nanostructures with semiconductor nanoparticles (NPs) to form hybrid plasmon–exciton nanoscale assemblies can potentially lead to plasmon-induced optical activity and unusual chiroptical properties of plasmon–exciton states. Here we investigate such effects in supraparticles (SPs) spontaneously formed from gold nanorods (NRs) and chiral CdTe NPs. The geometry of this new type of self-limited nanoscale superstructures depends on the molar ratio between NRs and NPs. NR dimers surrounded by CdTe NPs were obtained for the ratio NR/NP = 1:15, whereas increasing the NP content to a ratio of NR/NP = 1:180 leads to single NRs in a shell of NPs. The SPs based on NR dimers exhibit strong optical rotatory activity associated in large part with their twisted scissor-like geometry. The preference for a specific nanoscale enantiomer is attributed to the chiral interactions between CdTe NP in the shell. The SPs based on single NRs also yield surprising chiroptical activity at the frequency of the longitudinal mode of NRs. Numerical simulations reveal that the origin of this chiroptical band is the cross talk between the longitudinal and the transverse plasmon modes, which makes both of them coupled with the NP excitonic state. The chiral SP NR–NP assemblies combine the optical properties of excitons and plasmons that are essential for chiral sensing, chiroptical memory, and chiral catalysis.

KEYWORDS: Chiral assemblies, supraparticles, nanoscale chirality, hybrid electronic states, polarization rotation, circular dichroism



Nanoscale assemblies comprising both semiconductor and metal nanoparticles (NPs) have attracted a great deal of attention over the past decade because of the possibility of plasmon–exciton hybridization. A variety of synthetic techniques have been used to prepare such NP assemblies taking advantage of chemical or biological conjugation,^{1–4} electrostatic attraction,^{5–7} templates,^{8,9} and solvophobic interactions.^{10–12} The hybridized electronic states characteristic of both types of nanoscale materials in these diverse metal–semiconductor assemblies displayed unusual optical, catalytic, and magnetic properties^{13–18} with both fundamental and practical significance.

Concomitantly, there has been a rapid increase in the number of studies related to the preparation and characterization of chiral assemblies of semiconductor and metallic NPs. Chirality—a scale-less geometric attribute—translates into a number of useful functional properties of molecules, individual NPs, and their assemblies. Among them, molecular recognition

of chiral isomers and differential interactions with polarized light are primary examples of distinct chemical and physical properties related to chirality. Nanoscale particles, films, and assemblies reported recently exhibit the strongest known polarization rotation of visible electromagnetic radiation due to efficient coupling with the spin angular momentum of incident photons.^{19–21} The potential applications of chiral NPs and their assemblies include biosensing,^{22,23} enantioselective separations,²⁴ catalysis,²⁵ memory devices,²⁶ and polarized light-emitting diodes.²⁷ Most often, the chirality of these NP assemblies has a biological origin and is derived from the helical geometry of the DNA- or polymer-based “scaffolds” to which the NPs are attached.^{28,29} Chiral geometries of NP assemblies can also be obtained using careful ab ovo design of NPs

Received: June 14, 2014

Revised: October 3, 2014

Published: November 17, 2014



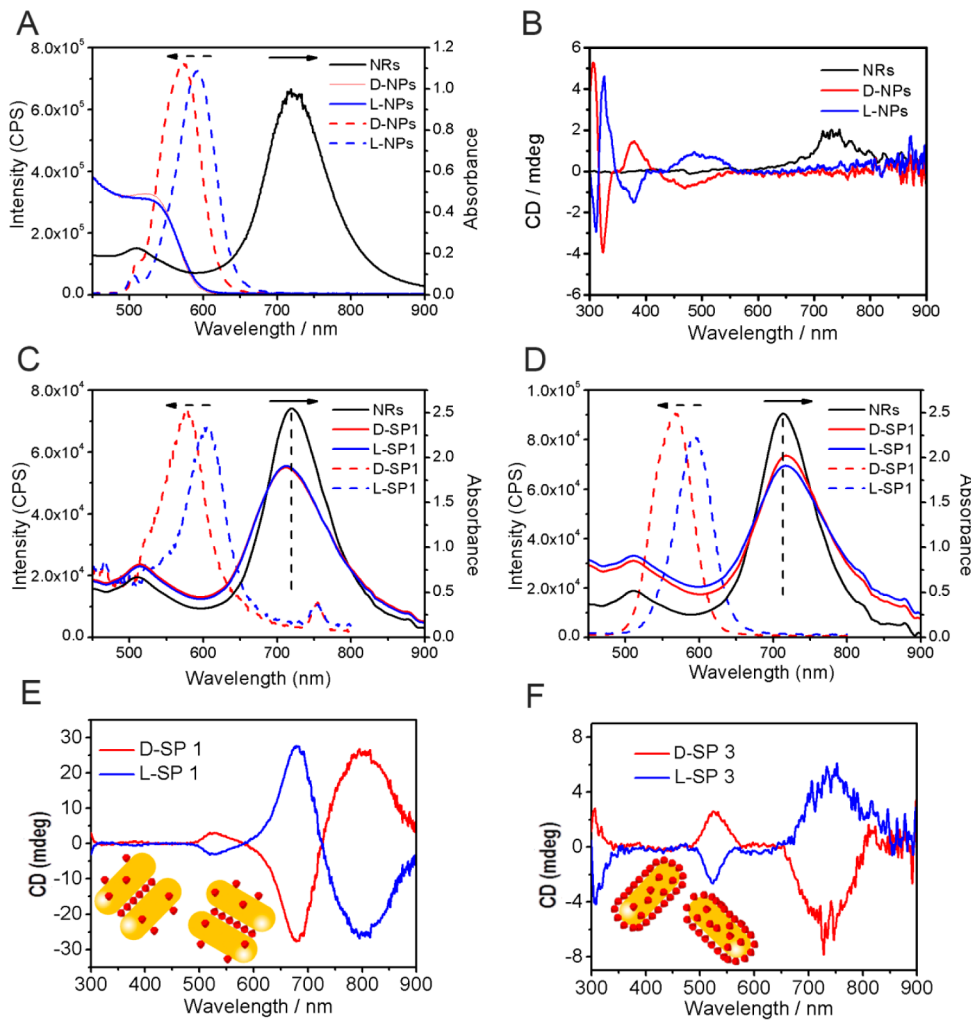


Figure 1. (A) UV–vis–NIR absorption (solid line) and photoluminescence (dashed line) spectra ($\lambda_{\text{ex}} = 380$ nm) of the original chiral CdTe NPs and gold NRs; (B) CD spectra of the original chiral CdTe NPs and gold NRs; (C) UV–vis–NIR absorption (solid line) and photoluminescence (dashed line) spectra ($\lambda_{\text{ex}} = 380$ nm) of the original NRs and chiral SP assemblies d-SP1 and l-SP1; (D) UV–vis–NIR absorption (solid line) and PL (dashed line) spectra ($\lambda_{\text{ex}} = 380$ nm) of the original NRs and chiral supraparticle assemblies d-SP3 and l-SP3; (E) CD spectra of the chiral SP assemblies d-SP1 (red) and l-SP1 (blue); the inset is a schematic representation of the proposed structure of SP1; (F) CD spectra of the chiral SP assemblies d-SP3 (red) and l-SP3 (blue); the inset is a schematic representation of the proposed structure of SP3.

assemblies by arranging NPs in space following a particular three-dimensional (3D) pattern exemplified by tetrahedral,^{30–32} helical,^{33,34} and twisted-rod patterns.^{22,23,35,36}

Expansion of the toolbox of NP assemblies toward simpler and more versatile synthetic techniques will increase the utility of chiral plasmonic, excitonic, and hybridized^{37,38} systems. With the exception of two recently published studies on systems synthesized by bioconjugation,^{31,39} little is known about the chiroptical effects of combining semiconductor and metal NPs into a chiral superstructure. Observations from organic dyes have suggested the enhancement of chiral anisotropy results from interactions between polarized light and chiral superstructures in a plasmonic field.^{40,41} The plasmonic field in these cases were generated by a single metal NP even though the strongest enhancements typically occur in gaps between plasmonic NPs.⁴² Considering the similarity of the molecular origin of chiral states in semiconductor NPs and organic molecules,⁴³ it may be possible to observe plasmonic enhancement of optical activity of NPs experimentally and computationally.^{25,44–46}

From this perspective, self-assembling supraparticles (SPs) offer fruitful grounds for the studies of chiral nanomaterials for multiple reasons. First, their size typically falls in the 100–200 nm range, which is convenient for effective coupling with visible light.⁴⁷ Second, the assembly process of terminal SPs is simple and versatile. It takes advantage of generic electrostatic and van der Waals attractive forces and can be applied both to metallic and semiconductor nanocolloids.⁴⁷ Third, the spatial proximity of the constituent NPs in SPs promotes effective resonance coupling between different electronic levels^{3,48–51} offering a versatile platform for plexcitonics^{52–55} and quantum plasmonics. Fourth, the shape of self-assembled SPs is not limited to spheres and can potentially result in asymmetric assemblies leading to chiral nanoscale superstructures.

Thus, we hypothesized that the preparation of chiral exciton–plasmon superstructures could be accomplished using SP assembly from chiral building blocks. Indeed, we made SPs based on achiral gold nanorods (NRs) and chiral CdTe NPs stabilized by L- and D-cysteine (CYS). Besides proving the original hypothesis, we uncovered several unexpected structural and optical effects in these structures.

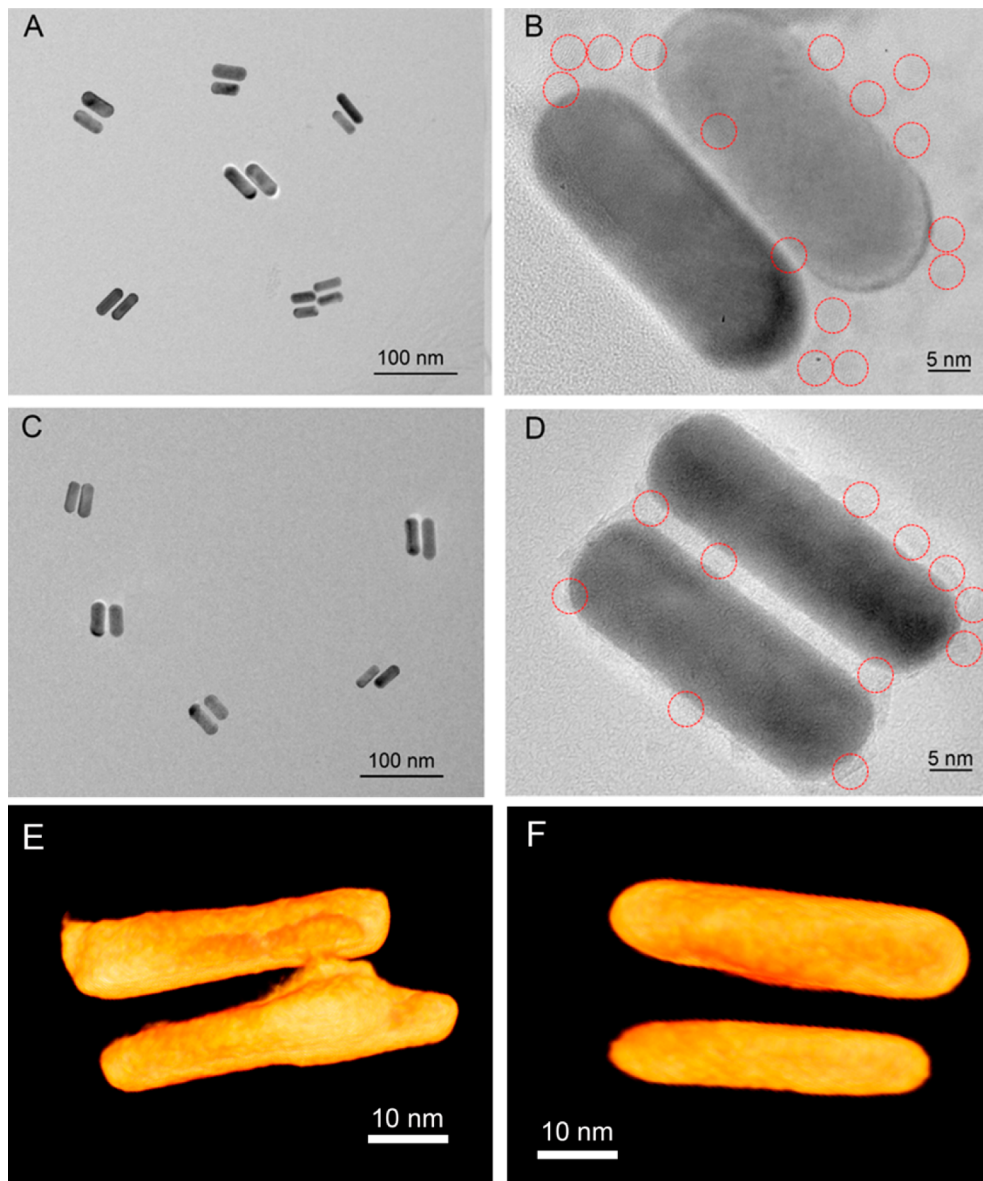


Figure 2. TEM images of the chiral SP assemblies SP1. (A) TEM image of D-SP1; (B) HRTEM image of D-SP1; (C) TEM image of L-SP1; (D) HRTEM image of L-SP1; (E) TEM tomography image for D-SP1. The presence of the most dense part of the CdTe coat is visible in the lower NR; (F) TEM tomography image for L-SP1. Visualization of the CdTe NP coat that lower e-beam contrast than gold, depends on the tomography and image rendering settings. The red circles in B and D indicate the positions of obvious CdTe NPs. Additional video files with 3D representation of the twisted pairs are given in the Supporting Information.

We observed two distinct modes of SP assemblies—with the core made from either one or two NRs surrounded by CdTe NPs—depending on the assembly conditions. SPs with a double-NR core acquire a geometry of twisted rods. The mirror image of this nanoscale superstructure is nonsuperimposable with the original and leads considerable enhancement of chiroptical activity. Unlike previous cases of similar scissor-like NR superstructures based on DNA^{22,23,36} or helical fibers,⁵⁶ self-assembly of such SPs is attributed to chiral intermolecular interactions of constitutive CdTe NPs forming the shell around the NRs that were recently shown to serve as structure-determining factor in assemblies of similar CdTe NPs.⁵⁷ A description of the chiroptical properties of single- and double-NR assemblies using electrodynamic simulations reveals complexity of plasmon–exciton interactions in the metal–semiconductor system. In the present study, this is exemplified

by the existence of significant “cross-talk” between the longitudinal mode and transversal plasmonic modes of gold NRs and their hybridization with chiral excitonic states in surrounding CdTe NPs.

Results and Discussion. Assembly of Gold NRs and Chiral CdTe NPs. Gold NRs and CdTe NPs were chosen as SP building blocks because their optical properties include strong absorption and emission peaks and energy overlap between excitonic and plasmonic states. Chiral CdTe NPs were prepared in two enantiomeric forms using established methods,⁴³ denoted here as L-NP and D-NP, using L- or D-cysteine (CYS) stabilizers, respectively. Figure 1A shows typical absorption and photoluminescence (PL) spectra of L-NP and D-NP; the sharp absorbance and PL peaks indicate the relatively narrow size distribution of the as-prepared NP samples. As expected, mirror image peaks are observed in the CD spectra

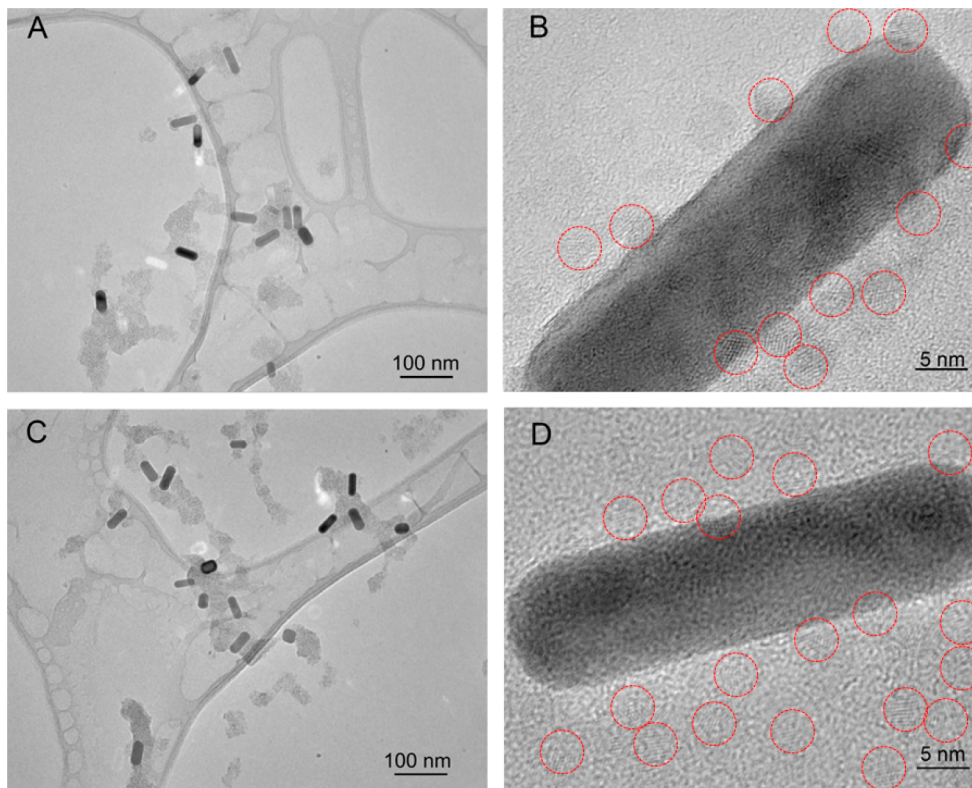


Figure 3. TEM images of the chiral SP assemblies SP3. (A) TEM image of d-SP3; (B) HRTEM image of d-SP3; (C) TEM image of l-SP3; (D) HRTEM image of l-SP3.

for L-NP and D-NP (Figure 1B), though the UV-vis-NIR spectra are nearly identical (Figure 1A). Gold NRs were prepared by a seed-mediated surfactant-directed approach. The NR transverse plasmon peak is at 520 nm, and the longitudinal plasmon peak is at 720 nm (Figure 1A), which is characteristic of length-diameter ratio of about 3:1. The TEM images in Figures 2 and 3 confirm this aspect ratio and show the gold NRs to be 15 nm in diameter and 45 nm in length.

The formation of SPs was achieved by adding chiral NPs to NRs in solution. To realize different assembly configurations, various quantities of chiral NPs were added to 2 mL of NR solution at room temperature. Three NR-NP molar ratios were used, 1:15, 1:60, and 1:180, and the resulting assemblies will be referred to as SP1, SP2, and SP3, respectively, with D- and L-prefixes indicating SPs assembled from D-NPs and L-NPs, respectively. After adding NPs to the NR solution, the self-assembly process was monitored by circular dichroism (CD) spectroscopy. The CD signal was recorded every 10 min, and the signal increased with time until the chiral SP assemblies of NRs and chiral CdTe NPs reached a steady state after 20 min (Figure S1). Subsequently, all samples characterized by CD, UV-vis-NIR, PL, and TEM measurements were prepared with a 20 min incubation following the initial mixing of the NPs and NRs.

While the CYS-capped D-NPs and L-NPs are optically active below \sim 510 nm (Figure 1B), the SP3 assemblies instead show two pronounced CD peaks at 520 and 720 nm (Figure 1F). It should be noted that, in Figure 1B, the small peak in the original NR CD spectrum at around 750 nm is associated with the likely presence of L-ascorbic acid ligands on the NRs before SP assembly; we do not consider this peak in our interpretation of the CD spectra of the SPs, although in some other systems

where the NRs are assembled by, for instance, ionic interactions, the chiral geometries associated with L-ascorbic acid ligands and their optical shifts might be essential.²² The SP3 CD peaks at 520 and 720 nm (Figure 1F) appear at the same positions as the transverse and longitudinal plasmon modes of the NRs, respectively (Figure 1A). Importantly, the CD spectra of L-SP3 and D-SP3 are mirror images of each other (Figure 1F) as expected for corresponding enantiomers.

In the course of the study, we observed a distinct difference in spectral features between the CD spectra of SP assemblies prepared with different molar ratios (Figures 1E and F, Figure S4A). While only peaks at 520 and 720 nm appear for SP3 (Figure 1F), the CD peaks for SP1 are much stronger and appear at 520, 678, and 801 nm. The CD spectra of SP2, which was made with an intermediate NR-NP ratio, reveal similarities with both SP1 and SP3 although revealing its own chiroptical features. All of these facts indicate that the origin of chiroptical bands in SP1 and SP3 are different and should be associated with different nanoscale geometries.

We also calculated the anisotropic factor (*g*-factor) values for the relative amounts of NRs and NPs (Figure S2). The *g*-factors are defined as $\Delta\epsilon/\epsilon$ where $\Delta\epsilon = \epsilon_L - \epsilon_R$ and $\epsilon = \epsilon_L + \epsilon_R$, respectively, and ϵ is the molar extinction coefficient using nonpolarized light.⁵⁸ The range of *g*-factors for SP1 are from 1.45×10^{-3} to -1.54×10^{-3} , almost 15 times greater than those of SP3, which exhibited *g*-factors ranging from 0.09×10^{-3} to -0.09×10^{-3} .

Optical and Structural Characterization. To better understand the structure of different NR-NP ratios, the SP assemblies were examined by UV-vis-NIR spectroscopy, photoluminescence (PL) spectroscopy, dynamic light scattering (DLS), zeta-potential characterization, and transmission

electron microscopy (TEM). The representative UV-vis-NIR spectra demonstrate clear differences between SP1 and SP3 (Figure 1C and D, respectively). Relative to the longitudinal plasmon absorption band of bare NRs at 725 nm, the SP1 UV-vis-NIR peak is decreased and blue-shifted (Figure 1C). Such a change is characteristic of side-by-side (SBS) assemblies of NRs.^{6,59,60} On the other hand, the UV-vis-NIR spectrum of SP3 shows a similar decrease but a red-shift of the longitudinal plasmon absorption band (Figure 1D).

The nanoscale SP assemblies were investigated by TEM, which revealed that, for SP1, the majority of NRs do indeed assemble into SBS dimers (Figure 2) when the chiral CdTe NPs are electrostatically attracted to two NRs at the same time. This is consistent for both d-SP1 and L-SP1 (Figures 2A and C, respectively). In these TEM images, we found a large number (70%) of NRs in dimers surrounded by NPs, that agrees with the blue-shifted UV-vis-NIR spectra of SP1; some SPs based on single NR cores were observed as well. Though TEM was performed on dried samples, here we found that most of the NR dimers self-assemble in SP1 solution and drying effects contribute little to the formation of NR dimers.⁶¹ High-resolution TEM (HRTEM) further confirmed that the SP assemblies of NR dimers were induced by the chiral NPs (Figure 2B and D). Several hundreds of NPs are adsorbed around the NR dimers. In a mechanism similar to previous observations of NR dimers formed in the presence of sodium citrate,⁵⁹ here NR assembly results from electrostatic attraction between positively charged NR surfaces and negatively charged chiral NP surfaces. The separated peak in the CD spectrum of SP1 (Figure 1E) supports the existence of dimers since exciton theory predicts that excited-state levels will split into two levels (one symmetric and one antisymmetric) upon dimerization.

On the basis of TEM, the structure of SP3 is different from that of SP1 (Figure 3). In particular, SP3 does not contain NR dimers, other SBS assembled structures (e.g., ladders), or any other end-to-end (ETE) assemblies.^{6,62} Though a number of NRs were aggregated, the majority of the SP3 assemblies contain a single NR in the core (Figure 3A and C). Furthermore, the high-resolution TEM (HRTEM) image revealed that a large number of NPs surround each NR (Figure 3B and D). This observation of isolated NRs surrounded by NPs in SP3 indicates that the red-shift of the plasmon absorption band (Figure 1F) can be attributed to an increased index of refraction about the NRs and/or to exciton-plasmon hybridization.^{3,48–51}

The TEM images for the SP2 sample reveal complex agglomerates that can be described as a combination of NR monomers and NR dimers (Figure S5). Both L-SP2 and d-SP2 gave assemblies similar in organization and geometry.

Photoluminescence measurements of the solution phase provide a characterization of the assemblies complementary to UV-vis-NIR. As previously reported,⁶³ when NPs are attached to NRs, and NP emission is quenched due to charge transfer to the metal. Relative to the photoluminescence spectra of the original NPs (Figure 1A), the SP1 and SP3 assemblies demonstrate strong emission quenching (Figure 1C and D, respectively). This quenching is attributed to the great majority of NPs being adsorbed to NRs.

The solutions were further characterized by dynamic light scattering (DLS) and electrokinetic zeta-potentials (ζ). For the original NRs, two DLS peaks are observed (Figures S3A,B). The smaller size peak is attributed to the NR diameter: this doubles between bare NRs and SP1 (Figure S3C,D) but

remains unchanged for SP3 (Figure S3G,H). The bigger size peak, which is attributed to the NR length, was not changed markedly from the bare NRs to SP1 or SP3. Taken together, this indicates that SP1 is composed predominantly of SBS NR dimers while SP3 is composed mainly of monomeric NRs. For both SP1 and SP3, a third, even larger DLS size distribution peak appears, indicating the presence of larger NR aggregates in the mixture. This peak is particularly intense for SP2 (Figure S3G and S3H), indicating that a significant number of NRs are in large agglomerates. At the same time, the charge of the SP1 is decreased from that of the original NRs, presumably by the adsorbed, negatively charged NPs, though SP1 is still positive (Table 1). Meanwhile, the charge of the SP3 assemblies is

Table 1. Electrokinetic Zeta-Potential Values for NRs, NPs, and Their Assemblies

enantiomer	NRs	original NPs	NPs at pH 7	SP1	SP2	SP3
levorotatory	+55.3	-21.6	-12.4	30.9	-26.3	-45.3
dextrorotatory	+55.3	-24.5	-13.6	30.7	-29.2	-45.4

negative (Table 1), which means that more negatively charged NPs surround each NR in SP3 relative to SP1. For SP2, the size distribution peaks became much broader (Figure S3E,F), in accordance with the large aggregates in the TEM image (Figure S5). Although the assembly size was large, the charge on SP2 was negative and smaller than that of SP3 (Table 1), which fit with our experiment observation that the SP2 was not stable and precipitated after 6 h.

Assembly Mechanism of Hybrid Metal–Semiconductor SPs. Consistent with the previously proposed SP assembly mechanism,⁶⁴ the NRs have a net positively charged surface due to strongly adsorbed CTA⁺ ions along the side surface, and at the pH of almost 7, the chiral CYS-capped CdTe NPs have a negative surface charges as confirmed by zeta-potential measurements (Table 1).

For higher NR–NP ratios (e.g., 1:15 for SP1), the presence of NPs induces SBS assembly of NRs, and the negatively charged chiral NPs adsorb along the side surfaces of the NRs, leading to negatively charged NR surface that are electrostatically attracted to positively charged adjacent NRs, resulting in SP assembly in the geometry of SBS dimers. “Overcharging” of the surfaces upon adsorption of macromolecular species is well-known in the field of layer-by-layer assembly.⁶⁵ Being attracted to both adjacent gold surfaces, the CdTe NPs positioned in the middle serve as “bridges” between the two NRs in the assemblies.

At a NR–NP ratio of 1:60 (SP2), a greater number of negatively charged NPs are adsorbed along the NR side surfaces. The electrostatic repulsion between the NRs surrounded by the CdTe NPs begins to increase, as confirmed by the increasingly negative zeta-potential (Table 1). SPs with double-NR cores start reassembling into SPs with a single-NR core conformation (Figure S3E,F), as supported by TEM images (Figure S5). We also see a wider size distribution of the aggregates.

Upon further decreasing the NR–NP ratio to 1:180 (SP3), a large number of NPs adsorb on the side surfaces of each NR, separating the NPs into monomeric SPs. This agrees well with the TEM images (Figure 3A and C).

Chiroptical Activity of Different SPs. To better understand the origin of the optical activity of NR-based SPs (Figure 1E–

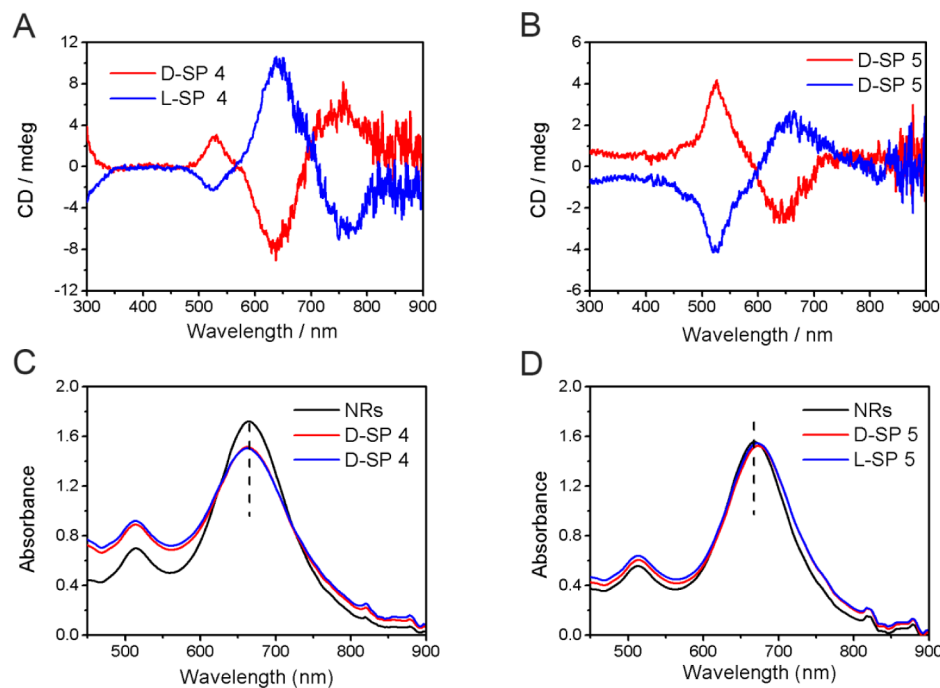


Figure 4. (A) CD spectra of the chiral SP assemblies D-SP4 (red) and L-SP4 (blue), (B) CD spectra of the chiral SP assemblies D-SP5 (red) and L-SP5 (blue), (C) UV-vis-NIR absorption of the original NRs and chiral SP assemblies D-SP4 and L-SP4; (D) UV-vis-NIR absorption of the original NRs and chiral SP assemblies D-SP5 and L-SP5.

F), new SPs were prepared from the same L- and D-NPs, but with shorter NRs (aspect ratio 2:1). The transverse plasmon peak of these shorter NRs is located at 520 nm, and the longitudinal plasmon peak is at 660 nm (Figure 4C). Two different NR–NP molar ratios were used, 1:10 and 1:120, and the resulting assemblies will be referred to as SP4 and SPS, respectively. Similar to SP1, TEM indicates that SP4 is a mixture of NR SBS dimer assemblies (60%) and NR monomer SPs (40%), while like SP3, SP5 is composed entirely of assemblies based on single-NR cores.

SP5 shows two CD peaks at 520 and 660 nm (Figure 4B), and like SP3, these two peaks agree well with the transverse and longitudinal SPR peaks, respectively, for the corresponding NR (Figure 4C). As was reported previously, chiral materials in a plasmonic field will have strongly enhanced CD at the plasmon frequency.^{44,66} By comparing the CD spectra of SP3 and SP5 (Figures 1F and 4B, respectively) to the measured absorbance of 3:1 and 2:1 NRs (Figures 1A and 4D, respectively), it is clear that the CD peaks are related to the NR localized surface plasmon modes, especially as the long-wavelength peak changes with the NR longitudinal plasmon resonance.

The CD peaks for SP4, which appear at 520, 640, and 758 nm, are much stronger than those of SP5 (Figure 4A). This is consistent with the trend for the 3:1 aspect ratio NRs: the CD spectrum of SP1 is also stronger than that of SP3. To discover the source of the strong optical activity that we measured for the SP1 and SP4 assemblies, TEM tomography was used to visualize the detailed 3D geometry of the NR dimers found in SP1 and SP4. By imaging these SBS dimers at multiple angles by TEM tomography (Figure 2E, F and Figure S6), we found that the two NRs of the assembly are not parallel. Rather, between the NR axes there is a clear dihedral angle, which we measured to be ca. 10°. Though parallel NRs will have a forbidden bonding mode for the coupled plasmonic states of individual NPs, this symmetry and selection rule is relaxed

when the two NRs are not exactly parallel, and the bonding mode is therefore not totally “dark” (i.e., the dipole moment is finite).²² Thus, for the SP1 and SP4 geometries, the CD spectrum is predicted to be the sum of the extinction band of this hybrid mode, and the rotational strength and direction of this CD spectrum can be described as $R = \text{Im}(\mathbf{p} \cdot \mathbf{m})$, where \mathbf{p} and \mathbf{m} are the electric and magnetic dipole moments of the plasmonic states, respectively.⁵⁶ Here, we only consider the electric dipole moments, so R only depends on the vector product of the two electric dipole moments,⁵⁶ and the expression can be reduced to $R = \pm (\pi/2\lambda)\mathbf{r}_{12} \cdot (\mathbf{p}_1 \times \mathbf{p}_2)$, where λ is the wavelength of the uncoupled plasmon and \mathbf{r}_{12} is the vector joining the two dipoles. If the two oscillating dipoles of the plasmonic states are parallel, \mathbf{r}_{12} is zero when the two oscillating dipoles have opposite directions (antisymmetric hybrid modes). However, the two dipoles are not parallel for the SP1 and SP4 assemblies, so \mathbf{r}_{12} is not zero for both of the symmetric and the antisymmetric hybrid modes, and so R changes sign between the two modes. This sign change means that the incident light polarization is rotated in different directions for the two modes and explains the bisignated line shape of the SBS dimer CD spectra (Figures 1E and 4A).

Physical Origin of Chiroptical Activity in NR-Based SPs. Finite difference time domain (FDTD) electromagnetic simulations confirmed the physical origins of the CD spectra for the SPs made from 3:1 NRs (SP1 and SP3) and the SPs made from 2:1 NRs (SP4 and SP5). The sizes and geometries of NRs, SBS dimer assemblies, and single-NR assemblies were taken from TEM (Figures 2, 3, and S6; Table S1). To account for heterogeneous SP mixtures in the experiments, appropriately weighted averages of the monomer and dimer spectra were used: SP1 was modeled as 70% SBS dimer assemblies and 30% NR monomer assemblies; SP3 was modeled as 100% NR monomer assemblies; SP4 was modeled as 60% SBS dimer assemblies and 40% NR monomer assemblies; and SP5 was

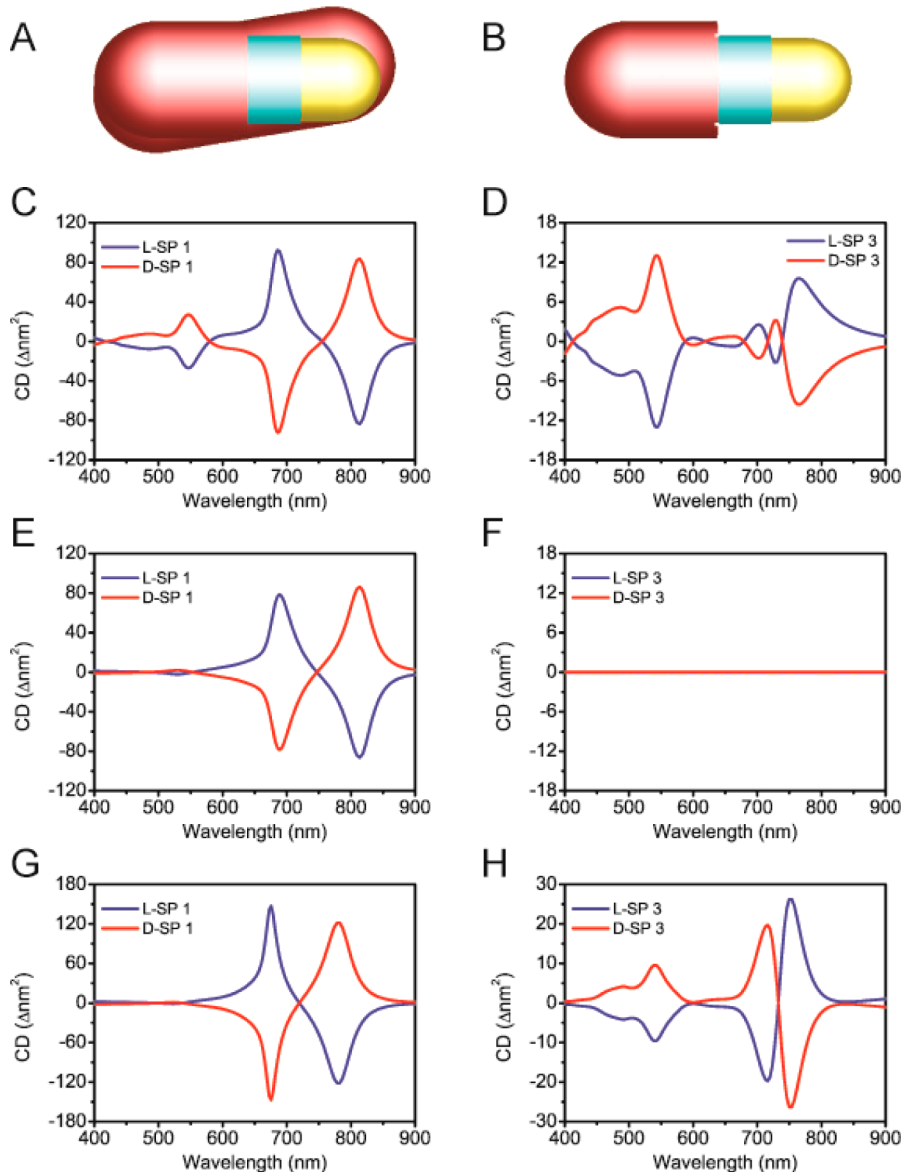


Figure 5. Simulated CD spectra for SP1 and SP3 assemblies. (A,B) Schematics of (A) SBS dimer and (B) NR monomer supraparticle models used in simulations. Yellow: 45×15 nm gold NR; blue: 0.5 nm spacer layer; red: 2.5 nm thick layer of adsorbed CdTe NPs. SP1 is modeled as 70% SBS dimer assemblies and 30% NR monomer assemblies; SP3 is modeled as 100% NR monomer assemblies. (C,D) SPs modeled with the measured refractive index and chirality of CdTe NPs (Figure S7B). (E) Simulated CD spectra of d-SP1 (red) and l-SP1 (blue); (F) simulated CD spectra of d-SP3 and l-SP3. (G) Simulated CD spectra of d-SP1 and l-SP1; (H) simulated CD spectra of d-SP3 and l-SP3. (I) Simulated CD spectra of 3:1 d- and l-SBS dimer assemblies with CdTe layer removed. (J) Simulated CD spectra of d-SP3 and l-SP3 with CdTe layer replaced by a chiral, but otherwise wavelength-independent, material (Figure S7C).

modeled as 100% NR monomer assemblies. The simulated geometries are depicted in Figures 5A and 6A. The monomer assemblies (Figures 5B and 6B for 3:1 and 2:1 NRs, respectively) are composed of a gold NR (yellow) surrounded by a 0.5 nm thick shell of water representing the surface ligands (blue) and a 2.5 nm thick shell of CdTe NPs (red). The SBS dimer assemblies (Figures 5A and 6A for 3:1 and 2:1 NRs, respectively) are composed of two monomer assemblies with a small dihedral angle relative to one another. Notably, both SP1 and SP4 revealed a dihedral angle of $\sim 10\text{--}15^\circ$. The reasons for consistency of the dihedral angle between two scissor-like assemblies investigated here as well as other chiroplasmonic NR assemblies studied before, is not quite clear at the moment.

The simulated CD spectra are presented in Figures 5 (SP1 and SP3) and 6 (SP4 and SP5). Here, CD is the differential extinction of left-handed and right-handed circularly polarized light, i.e., $CD = ext_{LHCP} - ext_{RHCP}$. To calculate the CD spectrum of d-SP1 (red curve in Figure 5C), the experimentally measured d-NP CD peak from 435 to 565 nm (Figure 1B) was added to the imaginary part of the refractive index for the CdTe NPs for excitation by LHCP light only, producing a chiral NP shell (Figure S7B). The simulated CD spectrum of l-SP1 (blue curve in Figure 5C) is provided for consistency with experiments; this is the negative of the CD spectrum of d-SP1. In excellent agreement with the experimental CD spectrum for SP1 (Figure 1E), the simulated spectrum for SP1 shows three peaks at $\lambda \approx 540, 690$, and 810 nm. Similarly,

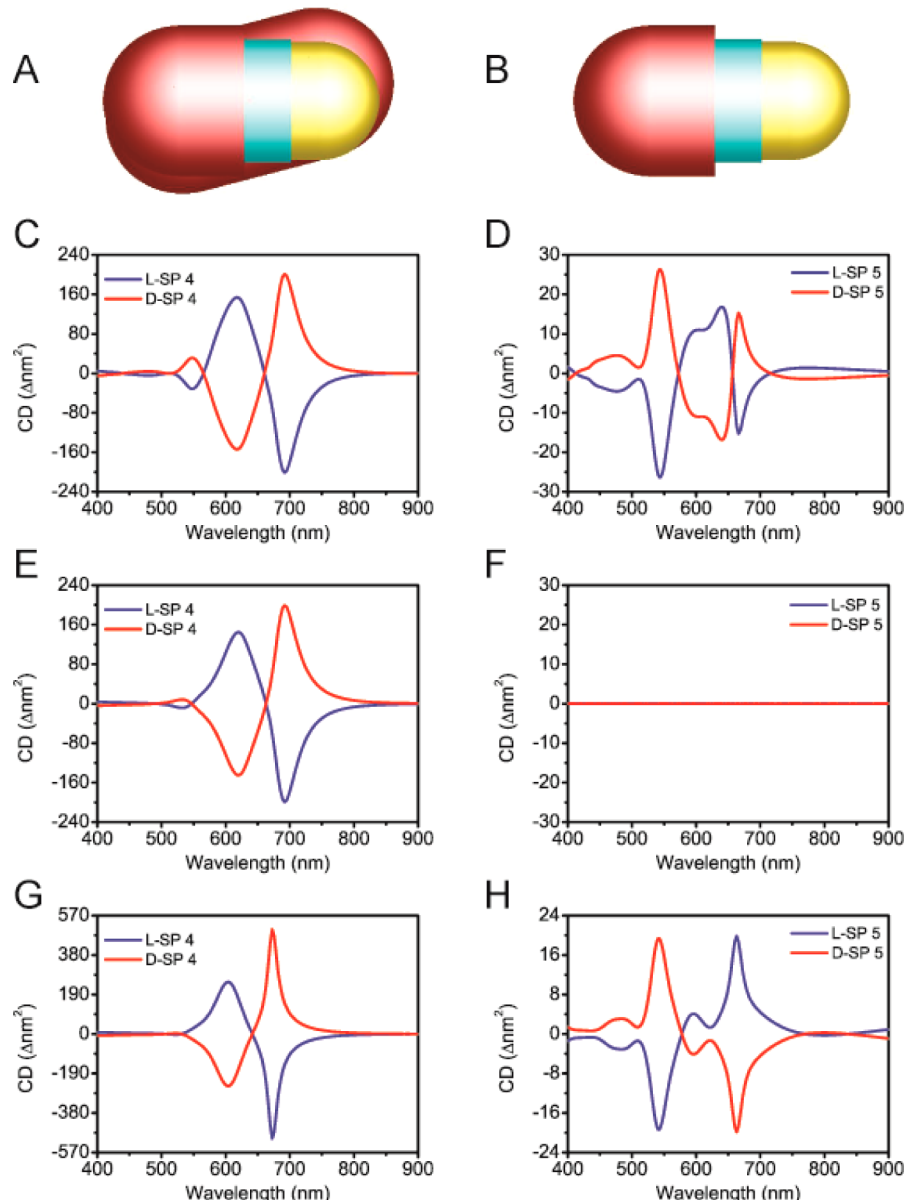


Figure 6. Simulated CD spectra for SP4 and SPS assemblies. (A,B) Schematics of (A) SBS dimer and (B) NR monomer supraparticle models used in simulations. Yellow: 47×22 nm gold NR; blue: 0.5 nm spacer layer; red: 2.5 nm thick layer of adsorbed CdTe NPs. SP4 is modeled as 60% SBS dimer assemblies and 40% NR monomer assemblies; SPS is modeled as 100% NR monomer assemblies. (C,D) SPs modeled with the measured refractive index and chirality of CdTe NPs (Figure S7B). (C) Simulated CD spectra of D-SP4 (red) and L-SP4 (blue); (D) simulated CD spectra of D-SP5 and L-SP5. (E,F) SPs modeled with the measured refractive index of CdTe NPs but no chiral absorption (Figure S7A). (E) Simulated CD spectra of D-SP4 and L-SP4; (F) simulated CD spectra of D-SP5 and L-SP5. (G) Simulated CD spectra of 2:1 D- and L-SBS dimer assemblies with CdTe layer removed. (H) Simulated CD spectra of D-SP5 and L-SP5 with CdTe layer replaced by a chiral, but otherwise wavelength-independent, material (Figure S7C).

the simulated CD spectrum for SP4 (Figure 6C) also successfully reproduces the corresponding experimental CD spectrum (Figure 4A). The CD spectra for SP1 and SP4 were both weighted averages of the CD spectra for monomer SPs and SBS dimer SPs. The extinction curves for these simulations are shown in Figure S8; these also correspond well to experiments.

To determine the source of the CD of SP1 and SP4, the simulations were repeated with the chiral NP shell replaced by an achiral NP shell (Materials and Methods; Figure S7A). The main features of the resulting CD spectra (Figures 5E and 6E for SP1 and SP4, respectively) are essentially unchanged from the CD spectra for SPs with chiral NP shells (Figures 5C and

6C). The small peaks at $\lambda \approx 520$ nm corresponding primarily to the chiroptical activity of NPs, predictably decrease. This indicates that the circular dichroism of the NPs does not produce the strong CD spectra of SP1 and SP4. To further probe the role of the NPs and to uncover any possible plasmon-exciton interaction, SBS NR dimer pairs were simulated without any CdTe layer at all, i.e., the SP geometries were left unchanged, but the NP shell was replaced by water. Remarkably, the shape of the CD spectra are preserved, though with the peaks slightly blue-shifted, as is expected due to the decreased local refractive index around the NRs (Figures 5G and 6G for 3:1 and 2:1 SBS NR dimer pairs, respectively). This indicates that the strong CD spectra of the SP1 and SP4

assemblies are not caused by the chiroptical activity of CdTe NPs per se. Also note that SP1 and SP4 contained a large number of SBS dimer assemblies, while SP3 and SP5 were composed nearly exclusively of single NR SPs. Therefore, the experimental CD spectra of these SPs (Figures 1F and 4B) cannot be explained simply with geometry as the monomeric NR is not geometrically chiral in isolation in the framework of this model.

The origin of the CD bands in SP1 and SP4 should therefore be attributed to the twisted cross-rod geometry of the SBS dimer SPs and is not to the “hot spot” enhancement of the chiroptical properties of chiral CdTe NPs. In other words, the difference in chiroptical activity of D-SP1 vs L-SP1 (and for D-SP4 vs L-SP4) comes not from the differences in chiroptical activity of individual D- and L-NPs, but rather from the chirality of the SBS assemblies as a whole. In turn, the latter originates from the chiral intermolecular interactions of NPs coated by L- and D-CYS stabilizers, which favor a NR twist in a particular direction. The evidence of the structure-determining role of the chiral interactions between NPs can be seen in the assemblies of CYS-stabilized CdTe NPs without the gold NRs. They form mesoscale helices with specific handedness depending on L- and D-form of CYS used to stabilize NPs (Supporting Information, Figure S10). A similarly strong indication that chirality of the NPs affects the geometry of the nanoscale assemblies is given in the recent study of the photoinduced assembly of CdTe stabilized by thioglycolic acid.⁵⁷ Note, in the latter case the stabilizer is achiral, and the enantioselectivity of the product—mesoscale twisted nanoribbons—originates from the chiral interactions characteristic of the inorganic core of the NPs. Both the molecular scale chirality of the stabilizer and the nanoscale chirality of the CdTe core are likely to play a role in chiral discrimination of the NR-based SPs with SBS geometry described in this study.

To further substantiate this attribution of chiroptical properties of SPs and to better understand light–matter interactions in these nanoscale assemblies, SP3 and SP5 were modeled using the optical properties for the CdTe NP shell about monomeric NRs (Figure S7B). On the basis of this material definition, the extinction spectra and corresponding CD spectrum were calculated for SP3 (Figure S8A and 5D, respectively) and for SP5 (Figure S8C and 6D, respectively). In the extinction spectra for SP3 (Figure S8B), we identify the peak at $\lambda \approx 520$ nm as the transverse plasmon mode (TM) and the peak at $\lambda \approx 730$ nm as the longitudinal plasmon mode (LM). In the corresponding calculated CD spectrum (Figure 5D), the main features are a broad dip at $\lambda \approx 540$ nm and a peak at $\lambda \approx 760$ nm. These match very well with the experimentally measured CD features shown in Figure 1F. Similarly, the experimental and simulated CD spectra for SP5 (Figures 4B and 6D, respectively) agree well. Unlike the case of SP1 and SP4, which contain SBS dimer assemblies, here, the simulated CD for SP3 and SP5 requires the chiroptically active CdTe NP shell: when these simulations of SP3 and SP5 were repeated with the chiral NP shell replaced by an achiral NP shell (Materials and Methods), no CD response was observed (Figures 5F and 6F, respectively).

Remarkably, despite the fact that the SP3 and SP5 shells reveal CD bands only from 435 to 535 nm, these monomeric SPs exhibit CD also at wavelengths strongly shifted to the red part of the spectrum. In order to explain this unanticipated result, we attribute some of these red CD signals to interactions between the transverse mode (TM) and the longitudinal modes

(LM) of the NR. Though the excitonic states of CdTe NPs and their CD peaks overlap spectrally only with the TM mode of the NRs, the TM and LM modes are not strictly orthogonal; there is some amount of intermodal “cross talk”. The presence of the NP coat can further enhance the cross-talk due to scattering of the plasmons on the field inhomogeneities produced by the proximal NPs. It should be noted that our computations involve only classical effects and are linear (no nonlinearities, e.g., saturation effects, are included). Thus, we account for the absorption of a given wavelength of light by an SP as the sum of three linear processes: (1) absorption by the CdTe layer, (2) direct absorption into the plasmon mode that is spectrally resonant with that light, and (3) indirect excitation of the second mode via “cross talk”. For example, in the case of SP3, 520 nm light can be absorbed “directly” to excite the TM, or the energy from the 520 nm excitation can be transferred from the TM to “indirectly” excite the 730 nm LM, while 730 nm light, which directly excites the LM, can also be absorbed “indirectly” into the TM.

The increased k for LHCP light incident on the CdTe NP shell (Figure S7B) has two effects on D-SP3: (a) CdTe absorbs LHCP excitation more strongly at $\lambda \approx 500$ nm and (b) the dielectric constant, $\epsilon = (n + ik)^2$, is increased. Increasing ϵ outside a metal NP decreases the skin depth and thus the amplitude of the plasmon oscillation. Therefore, under LHCP polarized light, the TM is weakened and thus absorbs less strongly. This second effect, (b), is expected to be more subtle than the first effect, (a).

Let us consider now the peak in the D-SP3 CD at 540 nm (Figure 1F). From (a) above, SP3 should absorb LHCP light more strongly than RHCP light because of increased k in the NP absorbance at that wavelength (Figure S7B). However, there is some decreased TM absorbance by the gold as suggested by (b) above. Furthermore, some of the 540 nm light is absorbed indirectly into the LM via the TM, and this absorption pathway is also slightly weakened because there is less TM absorbance. Still, because the effect of increased NP absorbance dominates, overall, LHCP 540 nm light is absorbed more strongly than RHCP 540 nm light, leading to a peak in the CD spectrum ($CD = ext_{LHCP} - ext_{RHCP}$).

Next, we consider the dip in D-SP3 CD at 750 nm (Figure 1F). At this longer wavelength, the CdTe absorbance is the same for LHCP and RHCP excitation light (Figure S7B), and because the dielectric constant of the NP shell is unchanged, the direct absorbance of the LM is also independent of polarization. Still, because some of the 750 nm light is indirectly absorbed into the TM via “cross talk” with the LM, and since this TM mode is weakened for LHCP light absorbance due to the increased dielectric constant at 540 nm, there is an overall decrease in absorption of 750 nm LHCP polarized light, leading to a dip in the CD spectrum ($CD = ext_{LHCP} - ext_{RHCP}$). This phenomenological description of the chiroptical activity of SP 3 can also be applied to the CD spectra of SP5 (Figure 4B).

Conclusions. In summary, we have investigated the formation and optical activity of terminal SP assemblies composed of gold NRs and chiral semiconductor NPs. When the molar excess of NPs is small (NR: NP = 1:10–1:15), the SPs are based on NR dimers with a scissor-like conformation. When the molar excess of NPs is large (NR: NP = 1:120–1:180), we observed a separation of the NR dimers into SPs based on single NRs due to increased electrostatic repulsion from a denser layer of adsorbed NPs. The chiral optical activity of the SPs based on NR dimers is attributed to the twisting of

NRs in respect to one other, leading to concomitant polarization rotation. Enantiomeric preference is associated in this case with chiral interactions between the NPs situated between the NRs. The optical activity of SPs with single-NR cores occurs due to the cross-talk between the longitudinal and transverse plasmonic modes of the NRs, with the latter being in resonance with the chiral exciton in the NPs. Note that this finding was possible due to the use of chiroplasmonic spectroscopy that enabled registration of distinct peaks corresponding to different excited states and therefore discrimination of different resonance phenomena. This experimental method can be further applied to other studies of electronic and energy transfer phenomena in complex plasmon-exciton systems. Besides the academic significance of identifying chiral exciton–plasmon states, the simplicity of preparation of SPs and similar terminal assemblies opens the door for further studies of chiral sensing, new polarization-based optical memory devices, and enantioselective catalysis.

Materials and Methods. *Materials.* Cadmium perchlorate hexahydrate ($\text{CdClO}_4 \cdot 6\text{H}_2\text{O}$) was purchased from Alfa-Aesar. Aluminum telluride powder (Al_2Te_3) was purchased from Materion Advanced Chemicals. Hydrogen tetrachloroaurate trihydrate ($\text{HAuCl}_4 \cdot 3\text{H}_2\text{O}$), L-ascorbic acid, silver nitrate (AgNO_3), sodium borohydride (NaBH_4), hexadecyltrimethylammonium bromide (CTAB), L-cysteine hydrochloride, and D-cysteine hydrochloride were purchased from Sigma-Aldrich. All chemicals are used as received. All chemicals used here were analytical grade or the highest purity available.

Measurements. CD spectra were recorded in aqueous solution by a JASCO J-810 spectropolarimeter. A portion of 2 mL of each sample was measured in a 1 cm quartz cell at a scan speed of 500 nm/min with a bandwidth of 10 nm, and the results were averaged over two consecutive scans. UV-vis–NIR absorption measurements were carried out using an Agilent 8453 spectrometer (300–900 nm), emission spectra were measured with a Fluoromax-4 spectrometer (Horiba Jobin Yvon) with excitation wavelength at 420 nm, and transmission electron microscopy (TEM) images were taken by JEOL-3011 transmission electron microscope. The hydrodynamic diameters of the supraparticles were determined by Malvern Zetasizer Nano ZS. The zeta-potentials were performed by the same instrument at room temperature.

Synthesis of Cysteine (CYS)-Capped CdTe NPs. CdTe NPs were prepared by reacting Cd^{2+} and H_2Te gas in the presence of chiral molecules as stabilizers according to the Rogach–Weller method⁶⁷ which we later modified.⁶⁸ A 0.498 g (0.59 mmol) sample of $\text{Cd}(\text{ClO}_4)_2 \cdot 6\text{H}_2\text{O}$ and 0.498 g (0.14 mmol) of (D,L)-cysteine was dissolved in 62 mL of distilled water. The pH was then adjusted to 11.2 by adding 1 M NaOH. The solution was placed in the three-necked flask and deaerated by N_2 gas for about 30 min. H_2Te gas generated by the mixture of 0.2 g of Al_2Te_3 , and 15 mL of 0.5 M H_2SO_4 in another three-necked flask was directed into the prepared solution under a N_2 atmosphere. The precursors were converted to CdTe nanocrystals by refluxing the reaction mixture at 100 °C for ~6–8 h in N_2 gas.

Synthesis of Gold Nanorods (NRs). Gold NRs were prepared from a seed-mediated, surfactant-directed approach described previously.^{69–71} Briefly, 0.25 mL of 0.01 M HAuCl_4 (0.0025 mmol) solution was added to 7.5 mL of a 0.1 M CTAB (0.75 mmol) solution, and the solutions were gently mixed. This was followed by addition of an ice-cold, 0.6 mL of aqueous 0.01 M NaBH_4 solution all at once, followed by rapid mixing

for 2 min. Then the gold seed solution was kept in a water bath maintained at 30 °C for 2 h. A 4 mL aliquot of 0.01 M HAuCl_4 , (0.04 mmol), 0.48 mL of 0.01 M AgNO_3 (0.0048 mmol), freshly prepared 0.48 mL of 0.10 M L-ascorbic acid (0.048 mmol), and 0.096 mL of CTAB-capped gold seed solution was synthesized beforehand and then were all added to 80 mL of 0.1 M CTAB, in that order, one by one, followed by thorough mixing after every addition. Finally, the gold NR suspension was left undisturbed at 30 °C overnight. The samples were purified by centrifugation (8000 rpm, 20 min) twice and redispersed in water before use.

FDTD Simulations. Electromagnetic simulations were performed using the commercial software package Lumerical FDTD Solutions. Gold NRs were modeled as cylinders with hemispherical end-caps. CdTe NP-conjugated NRs were approximated as a gold NR core surrounded by a 0.5 nm water layer representing the NR surface ligands, covered by a 2.5 nm thick CdTe NP film. GNR and SP geometries were taken from TEM (Table S1). The simulations were performed with a SP at the center of a simulation volume of $0.685 \mu\text{m}^3$, where near the SP a fine-mesh grid with a cell volume of 0.091 nm³ was used. Perfectly matched layer (PML) absorbing boundary conditions were used. The simulation was excited by a circularly polarized plane wave source from 400–900 nm, and scattering and absorption cross sections were measured in the particle near-field.

To simulate isotropically oriented particles in solution, all spectra were averaged over perpendicular excitation directions. UV-vis–NIR absorption measurements, which used incoherent light, were simulated by averaging the extinction spectra from right-hand and left-hand circular polarization excitation light (RHCP and LHCP, respectively). Circular dichroism was calculated as the difference between the extinction spectra for RHCP and LHCP excitation. To account for heterogeneous SP mixtures in the experiments, simulated spectra are presented as appropriately weighted averages of the monomer, and dimer spectra were used.

All SPs were simulated surrounded by water (constant refractive index of $n = 1.33$, $k = 0$). The same refractive index for Au was used for all simulations.⁷² Experimental ellipsometry data obtained from Prof. N. Gaponik for achiral CdTe NPs were used for the refractive index of achiral CdTe NP (SI, Figure S7A). CdTe optical activity was artificially introduced in our simulations of SPs by adding the experimentally measured D-NP CD peak from 435–565 nm (Figure 1B) to the imaginary part of the refractive index for the CdTe NPs for excitation by LHCP light, while the original CdTe refractive index was used for SPs excited by RHCP light (SI Figure S7B). The CdTe exciton was artificially removed by replacing the spectrally dependent n and k with a constant n and k equal to the average values. Here again, CdTe optical activity was artificially introduced by adding the experimentally measured D-NP CD peak from 435 to 565 nm (Figure 1B) to the imaginary part of the wavelength-independent refractive index for the CdTe NPs for excitation by LHCP light, while the original wavelength-independent CdTe refractive index was used for SPs excited by RHCP light (SI, Figure S7C).

ASSOCIATED CONTENT

Supporting Information

Time dependence of CD spectra for SP1 and SP3 (Figure S1); g-factor spectra of SP1 and SP3 (Figure S2); DLS spectra of the original gold NRs and of three SP assemblies (Figure S3); CD

and UV-vis-NIR absorption spectra of SP2 (Figure S4); TEM images of SP2 (Figure S5); TEM tomography image of d-SP1 at various tilt angles (Figure S6). Optical parameters of simulated CdTe NPs (Figure S7). Calculated extinction spectra (Figure S8). Sizes and geometries of simulated SP assemblies (Table S1). This material is available free of charge via the Internet at <http://pubs.acs.org>.

AUTHOR INFORMATION

Corresponding Authors

*E-mail: jsbiteen@umich.edu.

*E-mail: kotov@umich.edu.

Notes

The authors declare no competing financial interest.

ACKNOWLEDGMENTS

This work was largely supported by the Center for Photonic and Multiscale Nanomaterials (C-PHOM) funded by the National Science Foundation Materials Research Science and Engineering Center program DMR 1120923. The computational work was funded in part by a National Science Foundation CAREER award (CHE-1252322) to J.S.B. The funding for TEM studies came from the Center for Solar and Thermal Energy Conversion, an Energy Frontier Research Center funded by the U.S. Department of Energy, Office of Science, Office of Basic Energy Sciences under Award Number No. DE-SC0000957. We are thankful to Dr. Nikolai Gaponik from Technische Universität Dresden for spectral data for CdTe NPs. We appreciate the great help with TEM imaging given to us by Dr. Kai Sun and acknowledge the support of NSF Grant No. DMR-0315633 for the purchase of 3011 JEOL HRREM.

REFERENCES

- (1) Alivisatos, P. *Nat. Biotechnol.* **2004**, *22*, 47–52.
- (2) Yang, J.; Elim, H. I.; Zhang, Q. B.; Lee, J. Y.; Ji, W. *J. Am. Chem. Soc.* **2006**, *128*, 11921–11926.
- (3) Lee, J.; Govorov, A. O.; Dulka, J.; Kotov, N. A. *Nano Lett.* **2004**, *4*, 2323–2330.
- (4) Wang, T.; Zhuang, J. Q.; Lynch, J.; Chen, O.; Wang, Z. L.; Wang, X. R.; LaMontagne, D.; Wu, H. M.; Wang, Z. W.; Cao, Y. C. *Science* **2012**, *338*, 358–363.
- (5) Sarathy, K. V.; Thomas, P. J.; Kulkarni, G. U.; Rao, C. N. R. *J. Phys. Chem. B* **1999**, *103*, 399–401.
- (6) Chen, S. H.; Kimura, K. *Chem. Lett.* **1999**, 233–234.
- (7) Kalsin, A. M.; Fialkowski, M.; Paszewski, M.; Smoukov, S. K.; Bishop, K. J. M.; Grzybowski, B. A. *Science* **2006**, *312*, 420–424.
- (8) Kovtyukhova, N. L.; Mallouk, T. E. *Adv. Mater.* **2005**, *17*, 187–192.
- (9) Bai, F.; Wang, D. S.; Huo, Z. Y.; Chen, W.; Liu, L. P.; Liang, X.; Chen, C.; Wang, X.; Peng, Q.; Li, Y. D. *Angew. Chem., Int. Ed.* **2007**, *46*, 6650–6653.
- (10) Zhuang, J. Q.; Shaller, A. D.; Lynch, J.; Wu, H. M.; Chen, O.; Li, A. D. Q.; Cao, Y. C. *J. Am. Chem. Soc.* **2009**, *131*, 6084–6085.
- (11) Zhuang, J. Q.; Wu, H. M.; Yang, Y. A.; Cao, Y. C. *J. Am. Chem. Soc.* **2007**, *129*, 14166–14167.
- (12) Zhuang, J. Q.; Wu, H. M.; Yang, Y. G.; Cao, Y. C. *Angew. Chem., Int. Ed.* **2008**, *47*, 2208–2212.
- (13) Kuo, C. H.; Hua, T. E.; Huang, M. H. *J. Am. Chem. Soc.* **2009**, *131*, 17871–17878.
- (14) Seh, Z. W.; Liu, S. H.; Zhang, S. Y.; Bharathi, M. S.; Ramanarayanan, H.; Low, M.; Shah, K. W.; Zhang, Y. W.; Han, M. Y. *Angew. Chem., Int. Ed.* **2011**, *50*, 10140–10143.
- (15) Wang, C. G.; Chen, J.; Talavage, T.; Irudayarat, J. *Angew. Chem., Int. Ed.* **2009**, *48*, 2759–2763.
- (16) Sun, Z. H.; Yang, Z.; Zhou, J. H.; Yeung, M. H.; Ni, W. H.; Wu, H. K.; Wang, J. F. *Angew. Chem., Int. Ed.* **2009**, *48*, 2881–2885.
- (17) Wang, H. H.; Sun, Z. H.; Lu, Q. H.; Zeng, F. W.; Su, D. S. *Small* **2012**, *8*, 1167–1172.
- (18) Liu, M. Z.; Guyot-Sionnest, P. *J. Mater. Chem.* **2006**, *16*, 3942–3945.
- (19) Yeom, B.; Zhang, H.; Zhang, H.; Park, J. I.; Kim, K.; Govorov, A. O.; Kotov, N. A. *Nano Lett.* **2013**, *13*, 5277–5283.
- (20) Mark, A. G.; Gibbs, J. G.; Lee, T.-C.; Fischer, P. *Nat. Mater.* **2013**, *12*, 802–807.
- (21) Xia, Y. S.; Zhou, Y. L.; Tang, Z. Y. *Nanoscale* **2011**, *3*, 1374–1382.
- (22) Ma, W.; Kuang, H.; Xu, L. G.; Ding, L.; Xu, C. L.; Wang, L. B.; Kotov, N. A. *Nat. Commun.* **2013**, *4*, 2689.
- (23) Wu, X. L.; Xu, L. G.; Liu, L. Q.; Ma, W.; Yin, H. H.; Kuang, H.; Wang, L. B.; Xu, C. L.; Kotov, N. A. *J. Am. Chem. Soc.* **2013**, *135*, 18629–18636.
- (24) Shukla, N.; Bartel, M. A.; Gellman, A. J. *J. Am. Chem. Soc.* **2010**, *132*, 8575–8580.
- (25) Sawai, K.; Tatumi, R.; Nakahodo, T.; Fujihara, H. *Angew. Chem., Int. Ed.* **2008**, *47*, 6917–6919.
- (26) Fan, Z. Y.; Govorov, A. O. *Nano Lett.* **2010**, *10*, 2580–2587.
- (27) Naito, M.; Iwahori, K.; Miura, A.; Yamane, M.; Yamashita, I. *Angew. Chem., Int. Ed.* **2010**, *49*, 7006–7009.
- (28) Guerrero-Martinez, A.; Auguie, B.; Alonso-Gomez, J. L.; Dzolic, Z.; Gomez-Grana, S.; Zinic, M.; Cid, M. M.; Liz-Marzan, L. M. *Angew. Chem., Int. Ed.* **2011**, *50*, 5499–5503.
- (29) Zhu, Z. N.; Liu, W. J.; Li, Z. T.; Han, B.; Zhou, Y. L.; Gao, Y.; Tang, Z. Y. *ACS Nano* **2012**, *6*, 2326–2332.
- (30) Mastroianni, A. J.; Claridge, S. A.; Alivisatos, A. P. *J. Am. Chem. Soc.* **2009**, *131*, 8455–8459.
- (31) Yan, W. J.; Xu, L. G.; Xu, C. L.; Ma, W.; Kuang, H.; Wang, L. B.; Kotov, N. A. *J. Am. Chem. Soc.* **2012**, *134*, 15114–15121.
- (32) Chen, W.; Bian, A.; Agarwal, A.; Liu, L. Q.; Shen, H. B.; Wang, L. B.; Xu, C. L.; Kotov, N. A. *Nano Lett.* **2009**, *9*, 2153–2159.
- (33) Shen, X. B.; Song, C.; Wang, J. Y.; Shi, D. W.; Wang, Z. A.; Liu, N.; Ding, B. Q. *J. Am. Chem. Soc.* **2012**, *134*, 146–149.
- (34) Wang, R. Y.; Wang, H. L.; Wu, X. C.; Ji, Y. L.; Wang, P.; Qu, Y.; Chung, T. S. *Soft Matter* **2011**, *7*, 8370–8375.
- (35) Srivastava, S.; Santos, A.; Critchley, K.; Kim, K. S.; Podsiadlo, P.; Sun, K.; Lee, J.; Xu, C. L.; Lilly, G. D.; Glotzer, S. C.; Kotov, N. A. *Science* **2010**, *327*, 1355–1359.
- (36) Ma, W.; Kuang, H.; Wang, L. B.; Xu, L. G.; Chang, W. S.; Zhang, H. N.; Sun, M. Z.; Zhu, Y. Y.; Zhao, Y.; Liu, L. Q.; Xu, C. L.; Link, S.; Kotov, N. A. *Sci. Rep.* **2013**, *3*, 1934.
- (37) Lee, J.; Hernandez, P.; Lee, J.; Govorov, A. O.; Kotov, N. A. *Nat. Mater.* **2007**, *6*, 291–295.
- (38) Lee, J.; Govorov, A. O.; Dulka, J.; Kotov, N. A. *Nano Lett.* **2004**, *4*, 2323–233.
- (39) Nakashima, T.; Kobayashi, Y.; Kawai, T. *J. Am. Chem. Soc.* **2009**, *131*, 10342–10343.
- (40) Lieberman, I.; Shemer, G.; Fried, T.; Kosower, E. M.; Markovich, G. *Angew. Chem., Int. Ed.* **2008**, *47*, 4855–4857.
- (41) García-Etxarri, A.; Dionne, J. A. *Phys. Rev. B* **2013**, *87*, 235409.
- (42) Ward, D. R.; Grady, N. K.; Levin, C. S.; Halas, N. J.; Wu, Y.; Nordlander, P.; Natelson, D. *Nano Lett.* **2007**, *7*, 1396–1400.
- (43) Zhou, Y. L.; Yang, M.; Sun, K.; Tang, Z. Y.; Kotov, N. A. *J. Am. Chem. Soc.* **2010**, *132*, 6006–6013.
- (44) Govorov, A. O.; Fan, Z. Y. *ChemPhysChem* **2012**, *13*, 2551–2560.
- (45) Abdulrahman, N. A.; Fan, Z.; Tonooka, T.; Kelly, S. M.; Gadegaard, N.; Hendry, E.; Govorov, A. O.; Kadodwala, M. *Nano Lett.* **2012**, *12*, 977–983.
- (46) Maoz, B. M.; Chaikin, Y.; Tesler, A. B.; Bar Elli, O.; Fan, Z. Y.; Govorov, A. O.; Markovich, G. *Nano Lett.* **2013**, *13*, 1203–1209.
- (47) Xia, Y. S.; Nguyen, T. D.; Yang, M.; Lee, B.; Santos, A.; Podsiadlo, P.; Tang, Z. Y.; Glotzer, S. C.; Kotov, N. A. *Nat. Nanotechnol.* **2012**, *7*, 479–479.

- (48) Fofang, N. T.; Park, T. H.; Neumann, O.; Mirin, N. A.; Nordlander, P.; Halas, N. J. *Nano Lett.* **2008**, *8*, 3481–3487.
- (49) White, A. J.; Fainberg, B. D.; Galperin, M. *J. Phys. Chem. Lett.* **2012**, *3*, 2738–2743.
- (50) Wurtz, G. A.; Evans, P. R.; Hendren, W.; Atkinson, R.; Dickson, W.; Pollard, R. J.; Zayats, A. V.; Harrison, W.; Bower, C. *Nano Lett.* **2007**, *7*, 1297–1303.
- (51) Govorov, A. O.; Zhang, W.; Skeini, T.; Richardson, H.; Lee, J.; Kotov, N. A. *Nanoscale Res. Lett.* **2006**, *1*, 84–90.
- (52) Lee, J.; Hernandez, P.; Lee, J.; Govorov, A. O.; Kotov, N. A. *Nat. Mater.* **2007**, *6*, 291–295.
- (53) Lee, J.; Javed, T.; Skeini, T.; Govorov, A. O.; Bryant, G. W.; Kotov, N. A. *Angew. Chem., Int. Ed.* **2006**, *45*, 4819–4823.
- (54) Agarwal, A.; Lilly, G. D.; Govorov, A. O.; Kotov, N. A. *J. Phys. Chem. C* **2008**, *112*, 18314–18320.
- (55) Govorov, A. O.; Lee, J.; Kotov, N. A. *Phys. Rev. B* **2007**, *76*, 125308.
- (56) Auguié, B.; Alonso-Gómez, J. L.; Guerrero-Martínez, A. S.; Liz-Marzán, L. M. *J. Phys. Chem. Lett.* **2011**, *2*, 846–851.
- (57) Yeom, J.; Yeom, B.; Chan, H.; Smith, K. W.; Dominguez-Medina, S.; Bahng, J. H.; Zhao, G.; Chang, W. S.; Chang, S. J.; Chuvilin, A.; Melnikau, D.; Rogach, A. L.; Zhang, P.; Link, S.; Král, P.; Kotov, N. A. *Nat. Mater.* **2014**, Accepted.
- (58) Berova, N.; Di Bari, L.; Pescitelli, G. *Chem. Soc. Rev.* **2007**, *36*, 914–931.
- (59) Jain, P. K.; Eustis, S.; El-Sayed, M. A. *J. Phys. Chem. B* **2006**, *110*, 18243–18253.
- (60) Anna, L.; Aftab, A.; Diego, P.; Neil, C.; Jai, I. P.; Reuven, G.; Alexandre, G. B.; Eugenia, K. *J. Phys. Chem. C* **2012**, *116*, 5538–5545.
- (61) Nikoobakht, B.; Wang, Z. L.; El-Sayed, M. A. *J. Phys. Chem. B* **2000**, *104*, 8635–8640.
- (62) Ma, W.; Kuang, H.; Xu, L. G.; Ding, L.; Xu, C. L.; Wang, L. B.; Kotov, N. A. *Nat. Commun.* **2013**, *4*, 2689–2697.
- (63) Li, X.; Qian, J.; Jiang, L.; He, S. L. *Appl. Phys. Lett.* **2009**, *94*, 063111.
- (64) Orendorff, C. J.; Hankins, P. L.; Murphy, C. J. *Langmuir* **2005**, *21*, 2022–2026.
- (65) Decher, G. *Science* **1997**, *277*, 1232–1237.
- (66) Zhu, Z. N.; Guo, J.; Liu, W. J.; Li, Z. T.; Han, B.; Zhang, W.; Tang, Z. Y. *Angew. Chem., Int. Ed.* **2013**, *125*, 13816–13820.
- (67) Gaponik, N.; Talapin, D. V.; Rogach, A. L.; Hoppe, K.; Shevchenko, E. V.; Kornowski, A.; Eychmuller, A.; Weller, H. *J. Phys. Chem. B* **2002**, *106*, 7177–7185.
- (68) Zhou, Y. L.; Zhu, Z. N.; Huang, W. X.; Liu, W. J.; Wu, S. J.; Liu, X. F.; Gao, Y.; Zhang, W.; Tang, Z. Y. *Angew. Chem., Int. Ed.* **2011**, *50*, 11456–11459.
- (69) Nikoobakht, B.; El-Sayed, M. A. *Chem. Mater.* **2003**, *15*, 1957–1962.
- (70) Sau, T. K.; Murphy, C. J. *Langmuir* **2004**, *20*, 6414–6420.
- (71) Jana, N. R.; Gearheart, L.; Murphy, C. J. *Adv. Mater.* **2001**, *13*, 1389–1393.
- (72) Johnson, P. B.; Christy, R. W. *Phys. Rev. B* **1972**, *6*, 4370–4379.